Title

Structural dynamics of lytic polysaccharide monoxygenases reveals a highly flexible substrate binding region

Journal

Journal of Molecular Graphics and Modelling, 88(Biochemistry 56 20 2017)

ISSN

1093-3263

Authors

Arora, Radhika

Bharval, Priya

Sarswati, Sheena

et al.

Publication Date

2019-05-01

DOI

10.1016/j.jmgm.2018.12.012

Journal of Molecular Graphics and Modelling 88 (2019) 1–10

Contents lists available at ScienceDirect

Journal of Molecular Graphics and Modelling

journal homepage: www.elsevier.com/locate/JMGM

Structural dynamics of lytic polysaccharide monoxygenases reveals a highly flexible substrate binding region

Radhika Arora [a], Priya Bharval [a, 1], Sheena Sarswati [a, 1], Taner Z. Sen [b, c], Ragothaman M. Yennamalli [a, *]

[a] Department of Biotechnology and Bioinformatics, Jaypee University of Information Technology, Waknaghat, Himachal Pradesh, 173234, India
[b] U.S. Department of Agriculture, Agricultural Research Service, Crop Improvement and Genetics Research Unit, 800 Buchanan St., Albany, CA, 94710, USA
[c] Iowa State University, Department of Genetics, Development, and Cell Biology, Ames, IA, 50011, USA

ARTICLE INFO

Article history:
Received 5 September 2018
Received in revised form
3 December 2018
Accepted 18 December 2018
Available online 29 December 2018

Keywords:
Lytic polysaccharide monooxygenases
Elastic network models
Conformational dynamics
Bioethanol
Protein rigidity

ABSTRACT

Lytic polysaccharide monooxygenases (LPMOs), which are found in fungi, bacteria, and viruses, are redox enzymes utilizing copper to break glycosidic bonds in recalcitrant crystalline form of polysaccharides, such as chitin and cellulose. They are classified by the Carbohydrate-Active enZYmes (CAZy) database under various families. LPMOs's structure with a flat substrate binding region has been shown to contribute to its function, however, the role that LPMOs structural dynamics play during polysaccharide degradation and its mechanism of binding towards substrate are relatively unknown. Here, we report an exhaustive implementation of coarse-grained simulations using Elastic Network Models on multiple LPMO structures to shed light on how their structural dynamics contribute to their chemical function. Using Gaussian network models and Anisotropic network models, we show that the substrate binding region is highly flexible with significant and sustained micro-scale level conformational changes. Significantly, the loops on the binding side of the substrate are most mobile, in concert with the dynamic modes influencing the motions during binding. We also observed dynamic differences between four families of LPMO, namely AA9, AA10, AA11, and AA13 that consist of more than one structure. Specifically, the patterns of motion in the loop regions among the AA9 structures are distinct from those in the AA10 structures.

1. Introduction

It has been estimated that biomass utilization can replace 30% of current petroleum use [51,1], whose demand is continuously increasing in response to population increase and growing industrial and household needs worldwide. However, biomass processing is not as mature as petroleum processing, and has its own challenges in terms of substrate extraction, preparation, and treatment to facilitate and widen its usage. Cellulose, the most abundant biopolymer found in plant biomass, therefore presents itself as a unique and promising means to be used as substrate for biomass conversion into fuel [2], for a recent review please see Payne et al. [51].

Cellulose represents around 33% of vegetable matter (50% of wood and 90% of cotton are made of cellulose) [3]. Chitin is present in the exoskeletons of arthropods and as well as in the fungal cell wall. These two polysaccharides are both recalcitrant, i.e., naturally resistant in their crystalline form for enzymatic degradation [4]. For this reason, current biomass pretreatment processes involve converting the crystalline form of cellulose into an amorphous form for easy breakdown [5–7]. Nature also found numerous ways to break cellulose in plant cell wall via cellulases, a broad class of enzymes that degrade cellulose [8], among them are Lytic polysaccharide monooxygenases (LPMOs).

Lytic polysaccharide monooxygenases (LPMOs) have the capability to act on recalcitrant polysaccharides, such as chitin and cellulose. LPMOs are found in fungi, bacteria, and viruses. They are redox enzymes that use copper to cleave glycosidic bonds [9]. They are considered to be important contributors for the conversion of

* Corresponding author. Vivekananda Bhavan, 2nd Floor, Department of Biotechnology and Bioinformatics, Jaypee University of Information Technology, Waknaghat, Distt: Solan, Himachal Pradesh, 173234, India.
E-mail addresses: ym.ragothaman@juit.ac.in, ragothaman@gmail.com (R.M. Yennamalli).
[1] Equal authors.

https://doi.org/10.1016/j.jmgm.2018.12.012
1093-3263/

Abbreviations:

AA	Auxilliary Activity
CaZy	Carbohydrate-Active enZYmes
LPMO	Lytic polysaccharide monooxygenases

polymers, where they synergistically act with other hydrolytic enzymes for the breakdown of cellulose and chitin [10]. LPMOs were first discovered only in the last decade in *Serratia marcesences*, and classified as chitin binding proteins [11]. However, later studies established them as enzymes with redox activity [9,12–14], leading to a high interest in industrial applications (e.g., Cellic CTec2 from Novozymes is an enzyme cocktail, which includes LPMOs) [15,16].

The enzymes were initially classified as glycoside hydrolase family 61 (GH61) and carbohydrate binding module family 33 (CBM33) and then renamed as AA9, AA10, AA11, AA13, AA14, and AA15 families [17]. AA14 and AA15 family are recently classified LPMOs from white-rot and brown-rot basidiomycetes and *Thermobia domestica*, respectively [18,19]. As of September 2018, the AA9, AA10, AA11, AA13, AA14, and AA15 families consist respectively of 406, 3778, 99, 18, 15, and 253 sequences in the Carbohydrate-Active enZYmes (CAZy) database.

The structure of LPMO is an immunoglobulin-like distorted β-sandwich fold [20,21]. It consists of antiparallel β-strands, which are connected by loops with different number of α-helix insertions. Superposition of the structures from four families of LPMO, namely AA9, AA10, AA11, and AA13 (Fig. 1) shows that they share a high degree of structural similarity. Their substrate binding surface is reportedly a "flat" surface that consists of a divalent copper center that is surrounded by three nitrogens in a T-shaped geometry [13]. The main chain amino group of the N terminal histidine (His1) and imidazole side chain contribute two of its nitrogens and the second conserved histidine contributes the third nitrogen. Copper ions take electrons from an external electron donor, such as a reducing agent that is either provided by the substrate or by a cosecreted enzyme called cellobiose dehydrogenase and then reduces bound oxygen via internal electron transfer [23].

Since their discovery of boosting the yield of monosaccharides, LPMOs's unusually planar or "flat" substrate binding side has been the focus of multiple studies [10,14,24–26]. LPMOs's molecular architecture to bind to cellulose and chitin (and other polymers) is most likely evolved due to the presence of a diverse substrate landscape [10]. Vaaje-Kolstad et al. gave the first insight to the different mechanisms of LPMOs by using isotropically labeled dioxygen for the overall confirmation of monooxygenases activity on chitin and quantitative analysis of products formed using MADLI-TOF mass spectrometric method [14]. LPMOs are redox enzymes and hydrolyze the substrates. In the first step, LPMOs remove the hydrogen atom (bound to either C1 or C4) thereby creating an electron imbalance in the glycosidic bond, which leads to release of oxygen and breaking of the glycosidic bond.

LPMOs have been subcategorized into three different types (Fig. 2) based on the type of catalytic reactions by the Marletta group [27]. LPMOs have two types of reactions based on the abstraction of the hydrogen at the carbon atom positions (either C1 or C4) followed by glycosidic (C-O) bond cleavage, where enzymes specifically attacking the hydrogen at the C1 are called as type 1 LPMOs, and enzymes specifically attacking the hydrogen at the C4 are called as type 2 LPMOs (Fig. 2). Enzymes that do not have specificity to either C1 or C4, are called type 3 LPMOs [10]. Fig. 2 shows the schematic mechanism of the three types of LPMOs'sregiospecificity [27,28].

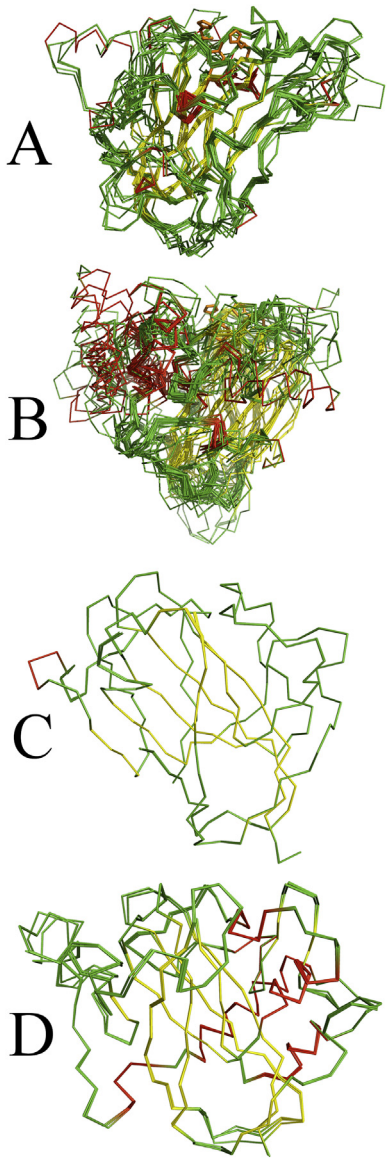

Fig. 1. Structural superposition of lytic polysaccharide monooxygenase (LPMO) (A) AA9 (24 structures with an average RMSD of 0.895 Å to the representative structure 2vtc), (B) AA10 (31 structures with an average RMSD of 3.267 Å to the representative structure 2bem), (C) AA11 (2 structures with a RMSD of 0.078 Å to the structure 4mah), and (D) AA13 (4 structures with an average RMSD of 0.190 Å to the representative structure 4opb). Structural superposition of the three families is shown to indicate the structural conservation of LPMOs. The coloring is based on secondary structure, where helices are colored red, β-strands are colored yellow, and loops are colored green. Image made using PyMOL [22].

Cumulatively, there are more than 70 PDB entries for LPMO across the families, and to date an exhaustive survey of structural dynamics analysis has not been conducted. Since, the amount of structural data for LPMOs is quite substantial, comparative structural studies have been reported. However, comparative analysis of structural dynamics would help in filling the gap in knowledge-base. Such studies help in comparative analysis of various structures within and across families. Due to high computation cost and time involved in a molecular dynamics (MD) simulation, the coarse-grained methods (such as Elastic Network Models (ENM)) are a simpler and cheaper alternative to do a structural dynamics study. ENM provides quantifiable data on residue level fluctuations that have biological and functional correlation [29]. Here, we

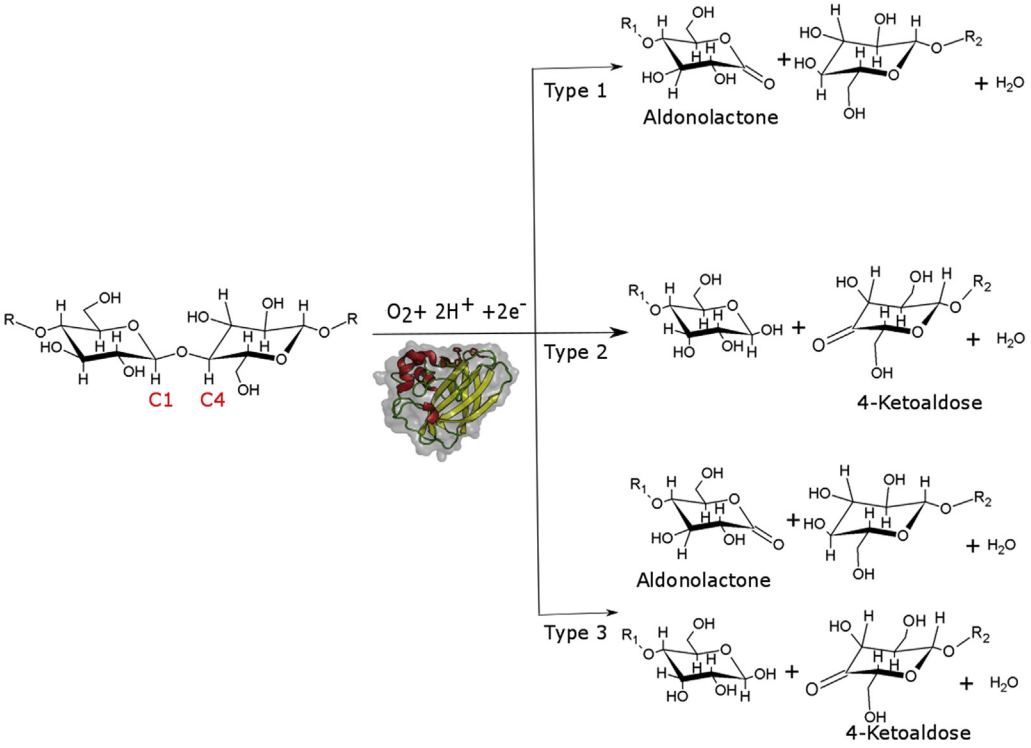

Fig. 2. LPMOs and their mechanism of action. Three types of LPMOs classified based on the site of attack. Image adapted from Ref. [10].

computationally analyze the currently known crystal structures of LPMOs and quantify their intrinsic dynamics, identify longer timescale motions that are highly likely to be biologically meaningful, and elucidate how dynamics can contribute specific LPMO mechanism of enzymatic action in comparison with experimental studies.

2. Results and discussion

2.1. Elastic network models highlight the biologically relevant motions

Elastic Network Model (ENM) approaches are normal mode analysis-based methods (NMA) that can provide functional information in a protein structure. ENM is used as the representation of NMA, where the fast and slowest modes of proteins or any biomolecules can be quickly quantified [30]. The higher-frequency fast modes of NMA indicate the localized highly fluctuating regions/residues. In contrast, the low-frequency slow modes of NMA indicate the globalized fluctuations in the entire molecule. These fast and slowest modes are calculated via building an ENM gives information about flexible and rigid regions within a protein structure. ENM can be simply described as study of harmonic potential wells by using analytical means and within a short time can provide the insight to more important dynamics of protein structures [31]. Two types of ENMs, which are frequently used, are the Gaussian Network Model (GNM [32]) and Anisotropic Network Model (ANM [29]).

GNM describes the fluctuation correlation in the protein and explores the magnitude of the protein fluctuations. GNM stores the normal mode data describing the intrinsic dynamics of the protein structure by generating a Kirchhoff matrix. Tirion's "single parameter model" for normal mode analysis (NMA) made the energy potential more simplified, which explained NMA with uniform harmonic motion [33]. Later, Bahar and co-workers produced a much simpler version of NMA, i.e., ENM. GNM was developed to study the contribution of topological constraints on the collective protein dynamics [32]. Thus, GNM is used for observation of global dynamic behavior. In GNM, the C^{α} carbon residues are represented as nodes in a network connected by springs (if within 7 Å radius), undergoing Gaussian distributed fluctuations [34]. According to GNM, these fluctuations are assumed to be influenced by neighboring atoms and their influence can be measured by the local packing density of residues around every single C^{α} residue [34]. Theoretical mean square fluctuations (MSF) are computed and compared against the experimental B-factors for the validation of GNM.

Although fast and powerful, GNM only takes contact distance as a scalar value, and disregards the contact directionality. In contrast, ANM extends GNM, and takes contact directionality into account and provides the modal motions in three-dimensional Cartesian coordinates. In mathematical terms, the distance in GNM is in the form of scalar whereas the distance in ANM is in a vector form and the product of these scalar values results in anisotropic fluctuations by picking up the second derivative of the potentials as for the displacement along any axis in a 3D space. Thus, ANM provides dimensionality, and also gives rise to excessively high fluctuations [29]. In spite of lower accuracy in local relative degrees of flexibility, ANM is superior for accessing directional mechanism of motion as it creates a $3N \times 3N$ Kirchhoff's matrix [35].

To understand how the intrinsic structural dynamics of the planar surface of LPMO, we used Gaussian Network Model (GNM) and Anisotropic Network Model (ANM) to derive the structural dynamics of LPMOs. While molecular dynamics (MD) simulations provide a precise atomic detail of LPMOs structural dynamics, ENM overcome the limitation of MD analyses by generating longer timescale dynamic patterns in a shorter duration. In the case of LPMOs, the availability of multiple AA9, AA10, AA11, and AA13 structures would necessitate the need of high-performance or GPU based computation power to run individual MD simulations to

cover larger time scale dynamics, and to be statistically significant multiple runs from the starting conformation would be necessary. Such practical issues can be overcome with coarse-grained simulations, specifically with GNM and ANM models, to gather data in a relatively shorter time. These coarse-grained models do not need any energy minimization techniques and require only the coordinates with B-factors as input.

2.2. Choosing relevant data sets and representable protein structures

Kundu et al. have showed that GNM models are more reliable if they have a correlation of experimental B-factor vs. MSF of 0.58 or higher [35]. From the GNM results of 61 structures, we identified 26 structures in total, consisting of 14 structures in AA9 (Protein Data Bank [36] (pdb) id: 2vtc, 2yet, 3zud, 4b5q, 4eir, 4qi8, 5acf, 5aci, 5acj, 5foh, 5tkf, 5tkg, 5tkh, and 5tki) and 10 structures in AA10 (pdb id: 2bem, 3uam, 4ow5, 4oy6, 4oy7, 4oy8, 4x27, 4x29, 4yn2, and 5vg0) which had a B-factor vs. MSF correlation value of 0.58 or higher (Table 1). In the case of AA11 and AA13 there was only one structure, 4mah and 5t7j, respectively, which had a B-factor vs. MSF correlation above 0.58 (Table 1).

Further, we categorized these structures into the proposed subtypes of LPMO to check if there is any correlation of the dynamic motions with the reaction mechanism. However, such classification did not provide clear connection of correlated motions based on reaction type. We further analyzed the multiple structures of LPMO that were deposited from single study and upon removing redundancy we ended up with the 12 structures. Specifically, seven structures in AA9 family (pdb id: 2vtc, 2yet, 4b5q, 4eir, 4qi8, 5acf, and 5tkf); three structures in AA10 family (pdb id: 2bem, 4oy6, and 5vg0); one structure each in AA11 and AA13 (4mah and 5t7j, respectively). The selected 12 LPMO structures were analyzed further by building ANM models.

2.3. Global cross-correlation in LPMOs show strong similarities

The global cross-correlation heat maps that are calculated based on all modes obtained from ANM are shown in Supplementary Fig. S1, Supplementary Fig. S2, Supplementary Fig. S3, and Supplementary Fig. S4 for AA9, AA10, AA11, and AA13 families, respectively. The cross-correlation values are given in Supplementary Table S1.

Here, the red regions show positive cross-correlation and blue regions show negative cross-correlation. Cross-correlation values in each plot range from −1.0 to +1.0. In the global cross correlation maps for all modes (slow and fast) of AA9 LPMO, consisting of seven AA9 structures (Supplementary Fig. S1and Table 2), we observed that there are similar positive and negative cross-correlations that are followed by all the structures. Specifically, residues 70–100 show positive peaks with residues 150–175, where these residues are part of two β-strands and the loop connecting the β-strands. Interestingly, these loops are spatially close to the active site residues. Supplementary Fig. S2 shows the global cross-correlation maps for all modes (slow and fast) of three AA10 LPMO structures (Table 3). Compared to AA9, AA10 structures do not share the pattern of correlated peaks. Specifically, the residues 80–120 have positive peaks with the C-terminus of the protein. Supplementary Fig. S3 shows the global cross correlation maps for all modes (slow and fast) of AA11 LPMO (pdb id: 4mah), where the positive peak correlation pattern is similar to those observed in AA9, and the regions are close to the active site. Finally, Supplementary Fig. S4

Table 1
Correlations of Gaussian Network Model (GNM) fluctuations against experimental B-factors. Correlation values for AA9, AA10, AA11, and AA13 are shown with respect to their Protein Data Bank (pdb) ids, where those in bold font show a B-factor correlation value of 0.58 or higher [35]. The lower the correlation is between the experimental B-factors and the computed MSF, the lower the degree of representation for the elastic model.

AA9 Family		AA10 Family		AA11 Family		AA13 Family	
PDB ID	Correlation	PDB ID	Correlation	PDB ID	Correlation	PDB ID	Correlation
2VTC	0.68	**2BEM**	0.63	**4MAH**	0.72	4OPB	0.52
2YET	0.67	2BEN	0.27	4MAI	0.49	5LSV	0.52
3EII	0.57	2LHS	NAN			**5T7J**	0.62
3EJA	0.49	2XWX	0.32			5T7N	0.41
3ZUD	0.70	2YOY	0.40				
4B5Q	0.83	2YOW	0.40				
4D7U	0.42	2YOX	0.28				
4D7V	0.35	**3UAM**	0.67				
4EIR	0.75	4A02	0.32				
4EIS	0.57	4ALC	0.52				
4QI8	0.64	4ALE	0.52				
5ACF	0.61	4ALQ	0.52				
5ACG	0.54	4ALR	0.53				
5ACH	0.45	4ALS	0.52				
5ACI	0.63	4ALT	0.52				
5ACJ	0.59	4GBO	0.36				
5FOH	0.87	**4OW5**	0.70				
5N04	0.57	**4OY6**	0.62				
5N05	0.55	**4OY7**	0.70				
5TKF	0.80	**4OY8**	0.60				
5TKG	0.72	**4X27**	0.67				
5TKH	0.80	**4X29**	0.62				
5TKI	0.76	4YN1	0.57				
5UFV	0.53	**4YN2**	0.64				
		5AA7	0.57				
		5FJQ	0.52				
		5FTZ	0.50				
		5IJU	0.55				
		5VG0	0.59				
		5VG1	0.18				
		5SWZ	0.41				

Table 2
Structural equivalent residues of AA9 family.

4QI8	2VTC	2YET	4B5Q	4EIR	5ACF	5TKF
1–6			1–6			
9					9	
14–23			14–23		21–25	
24–32		42–44	24–32	26–29	28–31	26–29
33		45	34		32	30
34–35			35–36	31–32	33–34	31–32
36	53		37	33	35	
37–38	54–55		39	34–35	36–37	34–35
39–43	56–60	53–57	41–44	36–40	38–42	36–40
45	64					
49–50	65–66	63	55			
53–54	69–70	66–67	57–58	53	52	53
56	72	69	60		54	55
57–62	73–77	72–75	61–66	56–61	55–60	56–61
63–64	79–80	76–77	68	62–63	61–62	62–63
65	81	78	69		63	
66–67	82–83	79–80	70–71			
68–72	89	86	72–76	84	78	84
73–81	92–99	87–95	77–85	85–93	79–87	85–93
82	100			94	88	94
83	101			95		95
84	102					
89–90		101–102				
92		104				
94–102	114–118	110–114	97–105	108–111	93–101	108–111
103–104	119–120	115–116	106–107		102–103	
105	121		108		104	
106–107	122–123		110		106	
108	124				107	
109	125					
115	130	129		122	113	
118	132					
120–121	140	139	123–124	132		
122–123	141–142	140–141	125–126	134		134
124	143	142	127			135
125–126	144–145	143–144	129	136–137	127–128	136–137
127–128	147	146	130–131	139	130	139
129–148	148–167	147–166	132–151	140–159	132–149	140–159
149–152	168–171	168–170	152–155	160–163	150–153	161–163
153–157	172–176	171–175	156–160	164–168	161–164	164–168
158–167	177–186	176–185	162–170	169–178	165–174	169–178
168			171	179	175	179
169	188	187	172			
170–171	189–190	188–189	174	183		183
172–173		191	176	184–185		184–185
178–179			179–180	188	185	188
181–187	200–204	200–202	182–188	190–196	187–193	190–196
188–192	205–209	203–207	189–193	197–201	195–198	197–201
194	211	209	195	203	200	203
195	212	210	196	204	201	
196		211	197	205	202	205
197				206		206
199				208		
200	216					209
201–207	217–223	217–221	206–210	213–216	209–213	211–216
208–212	224–228	222–226	211–215	217–221	215–218	217–221
213		227		222		222
214				223		223

shows the global cross-correlation maps for all modes (slow and fast) of AA13 LPMO (pdb id: 5t7j), where the residues 70–100 show positive cross-correlation with C-terminus (residues ~210 onwards).

Overall, the global cross-correlation maps show that there are similarities within the same family of structures, i.e., AA9 structures have similar cross-correlations peaks. However, AA9 cross-correlations are distinctly different to AA10 and AA13 family of LPMO structures. The only exception is AA11 structure, whose patterns of cross-correlation peak are similar to AA9.

Eigenvalues obtained by GNM and ANM approaches indicates the time-scale of motions [37]. The eigenvector-based fluctuations associated with small eigenvalues are localized motions on the protein structure. In contrast, fluctuations that are associated with larger eigenvalues are large-scale, i.e., global, motions correspond to the movement of domains along normalized eigenvectors. Domain motions happen in a larger time-scale than localized fluctuations. Classical molecular dynamics simulations, as opposed to steered molecular dynamics or similar types of simulations, need to be run prolonged times to reach the longer time-scales necessary to identify slow domain motions that are easily captured by normal mode analysis approaches [38]. Thus, visualizing the ANM modes

Table 3
Structural equivalent residues of AA10 family.

2BEM	4OY6	5VG0
28–32	43–47	32–36
33–41	48–56	38–45
42		46
44–49	71–76	54
49–52	77–79	57
53–55	81–83	58–60
56–59	85–87	61–64
60–63		65–68
69–70	97–98	
72–82	108–118	72–79
83–88		80–85
104–108	138–142	101–103
109–110	144	104–105
111–122	147–158	106–117
123		118
124–125	160–161	
127–129	163–165	
130–140	167–177	
146	178	
147–157	180–189	126–136
158–161		137–140
168–170	197–199	
171–190	203–222	149–167
191–194	223–226	169–171

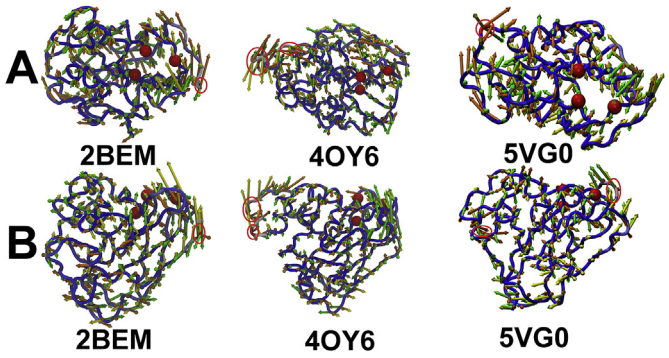

Fig. 4. First three slowest modes of AA10 LPMO for the proteins with the following PDB ids: 2bem, 4oy6, and 5vg0. **(A) Top view showing the active site residues as spheres with planar surface (B) Side view.** The first three slowest modes are plotted using NMwiz of VMD visualization tool [39]. The protein is shown as Cα trace, where the regions colored red are most mobile (red circles) and the regions colored blue are least mobile. The first slowest mode is represented with orange arrows, the second slowest mode is represented with yellow arrows, and the third slowest mode is represented with green arrows. The histidine and tyrosine/phenylalanine in the active site are shown as red spheres. (For interpretation of the references to color in this figure legend, the reader is referred to the Web version of this article.)

for the first three slowest modes in Figs. 3–6, we observed that certain regions of the protein are more flexible and dynamic in comparison to the rest of the structure.

Our results indicate flexibility, in general, around the substrate binding site of the protein. For instance, the structures belonging to AA9 (Fig. 3) have surface flexibility concentrated on one part of the protein. Specifically, the result of 4b5q correlates well with the reported MD simulations performed by Wu et al. where they showed that the loops closer to the substrate binding side are most mobile from a 100 ns MD simulation [40]. As shown in Figs. 3–6 the loop regions are relatively more dynamic than the other parts. However, other dynamic sites are observed in the non-substrate binding side of the protein. Also, the active site region (shown as red spheres in Fig. 3A and B) is less mobile than the loop regions, which indicates that the shape of the active site is crucial irrespective of the reaction type (type 1, 2, and 3) and the type of specific substrate (cellulose/chitin).

In order to understand the intricate dynamics that is happening in the LPMOs we took one LPMO from each family and looked into the positively and negatively cross-correlated regions and they are discussed in detail below.

2.3.1. Case study 1: AA9 LPMO

The AA9 LPMO from *Neurospora crassa* (pdb id: 4QI8) was taken as the test case, since *N. crassa* has been a well-studied organism in terms of biochemistry, genetics, and an annotated genome [41–44]. Among the regions that are positively cross-correlated (Supplementary Fig. S1), residue range 96–104 is correlated with residue range 62–70, which is part of the core of the protein structure forming β-strands, and interestingly the residues 62–70 are part of the substrate binding side of the protein. Another region that is positively cross correlated is residues 136–148 with residues 70–80, where these two regions form adjacent antiparallel β-strands stabilizing the core of the protein. A third positively cross-correlated region is spatially closer to the above two regions and is also part of the core.

2.3.2. Case study 2: AA10 LPMO

Among the many structures available for AA10 family of LPMO, we focused on one of the first crystal structures solved for this family from *Serratia marcescens* (pdb id: 2BEM). There are two large positively cross-correlated regions (Supplementary Fig. S2);

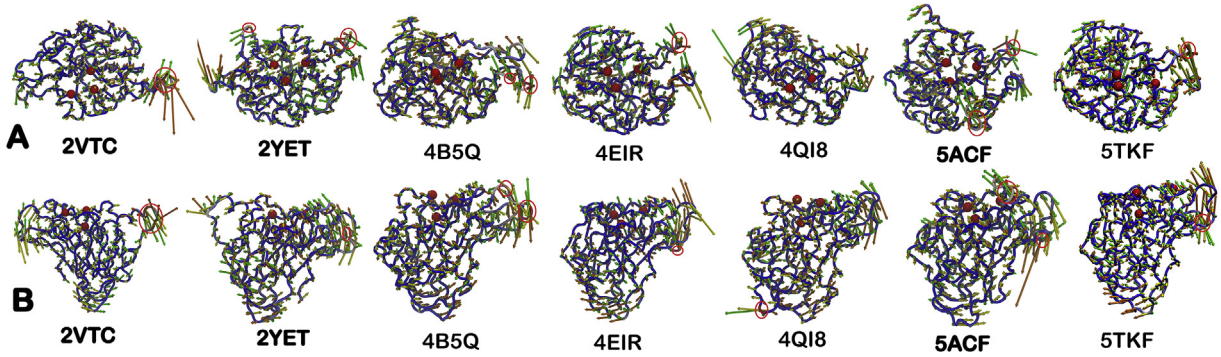

Fig. 3. First three slowest modes of AA9 LPMO for the proteins with the following PDB ids: 2vtc, 2yet, 4b5q, 4eir, 4qi8, 5acf, 5tkf. **(A) Top view showing the active site residues as spheres with planar surface (B) Side view.** The first three slowest modes are plotted using NMwiz of VMD visualization tool [39]. The protein is shown as C^{α} trace, where the regions colored red are most mobile (red circles) and the regions colored blue are least mobile. The first slowest mode is represented with orange arrows, the second slowest mode is represented with yellow arrows, and the third slowest mode is represented with green arrows. The histidine and tyrosine/phenylalanine in the active site are shown as red spheres. (For interpretation of the references to color in this figure legend, the reader is referred to the Web version of this article.)

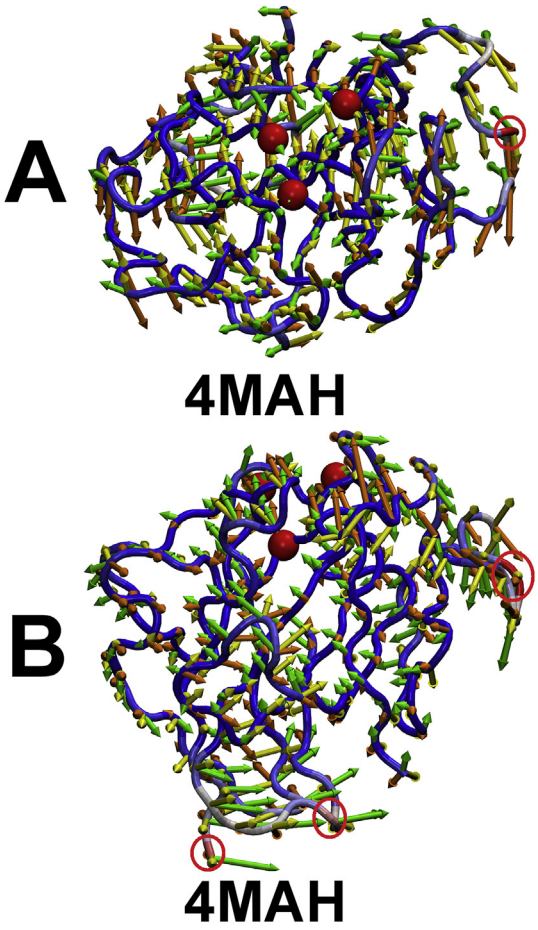

Fig. 5. First three slowest modes of AA11 LPMO for the protein with the PDB id 4mah. **(A) Top view showing the active site residues as spheres with planar surface (B) Side view.** The first three slowest modes are plotted using NMwiz of VMD visualization tool [39]. The protein is shown as C^{α} trace, where the regions colored red are most mobile (red circles) and the regions colored blue are least mobile. The first slowest mode is represented with orange arrows, the second slowest mode is represented with yellow arrows, and the third slowest mode is represented with green arrows. The histidine and tyrosine/phenylalanine in the active site are shown as red spheres. (For interpretation of the references to color in this figure legend, the reader is referred to the Web version of this article.)

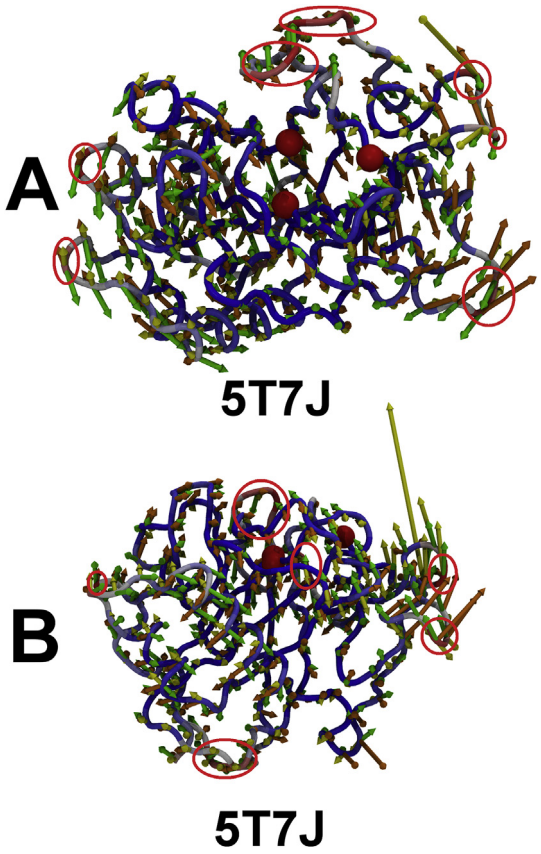

Fig. 6. First three slowest modes of AA13 LPMO for the protein with the PDB id 5t7j. **(A) Top view showing the active site residues as spheres with planar surface (B) Side view.** The first three slowest modes are plotted using NMwiz of VMD visualization tool [39]. The protein is shown as C^{α} trace, where the regions colored red are most mobile (red circles) and the regions colored blue are least mobile. The first slowest mode is represented with orange arrows, the second slowest mode is represented with yellow arrows, and the third slowest mode is represented with green arrows. The histidine and tyrosine/phenylalanine in the active site are shown as red spheres. (For interpretation of the references to color in this figure legend, the reader is referred to the Web version of this article.)

residues 172–182 correlated with 115–125 that are part of the protein core forming antiparallel β strands adjacent to each other. The other region consists of residues 185–192 correlated with 172–182 and forming β strand antiparallel in orientation within the protein core.

2.3.3. Case study 3: AA11 LPMO

The LPMO from *Aspergillus oryzae* (pdb id: 4MAH) is the sole LPMO that was selected, and it has three regions that are highly positively cross-correlated (Supplementary Fig. S3) and all these regions are located in the β strands of the protein core. The first region consists of residues 80–90 correlated with residues 60–65. Interestingly, the second region consisting of residues 127–136 is also correlated with residues 58–65. Also, the third region consists of residues 139–147 correlated with residues 123–130.

2.3.4. Case study 4: AA13 LPMO

The LPMO from *Aspergillus oryzae* (pdb id: 5T7J) is the sole LPMO selected and it has only one major region that is positively cross-correlated (Supplementary Fig. S4), specifically residues 213–221 in the β-strand in the protein core is correlated with 206–213 that form a loop not involved with substrate binding.

2.4. The dynamics of LPMOs: experimental vs. computational studies

LPMOs have been experimentally suggested to be rigid when bound to a metallic ion such as copper. Specifically, Aachmann et al. and Courtade et al. argued based on NMR relaxation studies that in the AA9 LPMO from *Serratia marcescens* and in the AA10 LPMO from *Neurospora crassa*, respectively have an inflexible backbone, more likely contributing to the electron transfer (ET) mechanism that LPMO is known to participate [23]. It has been widely accepted that proteins are rarely static in nature and have an inherent dynamics that influence its function and activity [45,46]. However, the "jiggling and wiggling" observed in general in most proteins has been reported to be missing or absent in LPMOs [47]. One explanation for this discrepancy is the timescale of observations: The timescales of the T1, T2, and NOE experiments reported are in the pico to nanosecond scale [48]. In contrast, large conformational changes in proteins are at the millisecond and longer timescales. Another possibility is as follows. Although the two NMR studies show flat metal binding site when bound to copper, the same studies show the same site flexible when not bound to copper. How

to explain this difference in bound and unbound dynamic simulations of LPMOs? Given that high structural similarity between bound and unbound structures in LPMOs, it seems as if elastic network models only capture the substrate binding side dynamics in the *absence* of copper, and, by not treating ionic bonds explicitly, overlook the effect of strong ionic bonds formed by copper binding. We calculated correlation between the B-factors and the mean-square fluctuations in the presence and absence of metallic ions represented as single nodes, and observed no difference between them (results are not shown). There is some recent evidence for the latter hypothesis: in 2018, Liu et al. performed molecular dynamics simulations, which treat ionic bonds explicitly, and observed that LPMO dynamics was somewhat reduced after binding to cellulose in the presence of copper [49]. We hope that future studies will shed more light on the dynamics of binding site.

3. Conclusions

Lytic Polysaccharide Monooxygenases (LPMOs) are a biologically exciting set of enzymes that help biomass degradation to produce bioethanol. Multiple families (AA9, AA10, AA11, AA13, AA14, and AA15) and three types of LPMOs have been identified, with regiospecific activity, and tertiary structures for multiple LPMOs are experimentally determined and deposited at Protein Data Bank (PDB). Here, we have provided the details about structural dynamics of four families of LPMOs (AA9, AA10, AA11, and AA13) by constructing Elastic Network Models (ENM) as they have more than one structure available for comparative study such as this one.

While the planar surface of LPMO has attracted attention with respect to the active site histidine-brace (made by the two histidines coordinated with a divalent metal ion), although the binding surface is important for specificity, other structural parts of LPMOs play a role in the dynamics of binding, and we observed that the loop regions surrounding the histidine-brace are relatively more mobile and the loop motions are in concert with the structural dynamics at the substrate binding side leading to structural changes needed for the enzyme to bind to a flat crystalline surface of the substrate, such as cellulose or chitin. Interestingly, we see similar motions in the slowest modes within each LPMO family, suggesting the importance of these modes in the functional dynamics of the substrate binding side. Many residues that are mapped to the binding side of the substrate of protein indicate their importance during binding.

4. Materials and methods

4.1. CAZy

CAZy is a database of Carbohydrate Active enzymes (CAZy), which provides information about the enzymes involved in the synthesis, transport, and metabolism of carbohydrates [17]. We have used this database to retrieve the information of the different families of LPMOs, i.e., AA9, AA10, AA11, AA13, which are tabulated in Supplementary Table 2 [17,20]. The respective LPMO structures we have downloaded from Protein Data Bank [36].

4.2. ProDy

ProDy is an open-source and free Python package [50]. It is used for protein structural dynamics analysis and is suitable for development of various applications and for the interactive sessions. ANM and GNM analyses were performed using ProDy. We generated different cross correlation maps and different output files using ProDy which were visualized in VMD [39]. Normal mode analysis is used for the representation of both the fast and slowest modes of a highly complex networked structure, such as a protein or any biomolecules [30].

4.3. GNM ***and ANM***

GNM [32] was developed to study the contribution of topological constraints on the collective protein dynamics, and ANM [29] provides motions along three coordinates. We used a C^{α} distance cutoff of 7.0 Å and a spring constant of one for building the GNM network. For ANM, the C^{α} distance cutoff of 13.0 Å was used. Detailed implementation of GNM and ANM in ProDy can be found in the following reference [50].

4.4. Correlation coefficient

To calculate the correlation between the experimental B-factors and computational mean-square fluctuations, we used the following linear correlation coefficient:

$$\text{Correlation coefficient} = \frac{\sum_{i=1}^{N}(x_i - \overline{x})(y_i - \overline{y})}{\sqrt{\sum_{i=1}^{N}(x_i - \overline{x})^2 \cdot \sum_{i=1}^{N}(y_i - \overline{y})^2}}$$

In this equation, N is the number of nodes, and x_i and $\overline{x}$ are the mean-square fluctuations of the ith node calculated by GNM and their mean over all nodes, respectively. Similarly, $y_i$and $\overline{y}$ are the experimentally determined B-factor for the ith node and the mean over all nodes.

Author contributions

RMY conceived the study and participated in the design and coordination and helped to draft the manuscript. RA, PB and SS conducted the study. PB analyzed and wrote the first draft of the manuscript and RA and TZS performed the final editing. The manuscript was written through contributions of all authors. All authors have given approval to the final version of the manuscript. ‡These authors (PB and SS) contributed equally.

Funding sources

This work was supported by the United States Department of Agriculture-Agricultural Research Service (project number 2030-21000-024-00D). The funding agency played no role in the design of the study and collection, analysis, and interpretation of data and in writing the manuscript. The authors also thank Mr. Pulkit A. Srivastava for helping in editing the manuscript.

Competing interests

The authors declare that they have no competing interests.

Conflicts of interest

The authors declare that they do not have any conflict of interest.

Acknowledgment

The authors wish to thanks Jaypee University of Information Technology for providing research and infrastructural facilities for this study. USDA is an equal opportunity provider and employer. The authors would like to thank Dr. Theresa Ramelot, Miami University for the discussions related to this manuscript.

Abbreviations

ANM	Anisotropic Network Model
GNM	Gaussian Network Model
NMA	Normal Mode Analysis
LPMO	Lytic Polysaccharide Monooxygenases

Appendix A. Supplementary data

Supplementary data to this article can be found online at https://doi.org/10.1016/j.jmgm.2018.12.012.

References

[1] R.D. Perlack, L.L. Wright, A.F. Turhollow, R.L. Graham, B.J. Stokes, D.C. Erbach, Biomass as Feedstock for a Bioenergy and Bioproducts Industry: the Technical Feasibility of a Billion-ton Annual Supply, DOE/GO-102005-2135, U.S. Department of Energy, Oak Ridge, TN, 2005.

[2] L.C. Duchesne, D.W. Larson, Cellulose and the evolution of plant life, Bioscience 39 (4) (1989) 238–241.

[3] W. Underwood, The plant cell wall: a dynamic barrier against pathogen invasion, Front. Plant Sci. 3 (2012).

[4] M.E. Himmel, S.-Y. Ding, D.K. Johnson, W.S. Adney, M.R. Nimlos, J.W. Brady, T.D. Foust, Biomass recalcitrance: engineering plants and enzymes for biofuels production, Science 315 (5813) (2007) 804–807, https://doi.org/10.1126/science.1137016.

[5] C. Alvarez, F.M. Reyes-Sosa, B. Diez, Enzymatic hydrolysis of biomass from wood, Microb. Biotechnol. 9 (2) (2016) 149–156.

[6] D.P. Maurya, A. Singla, S. Negi, An overview of key pretreatment processes for biological conversion of lignocellulosic biomass to bioethanol, 3 Biotech 5 (5) (2015) 597–609.

[7] M.Y. Wang, Z.H. Li, X. Fang, L.S. Wang, Y.B. Qu, Cellulolytic enzyme production and enzymatic hydrolysis for second-generation bioethanol production, in: Biotechnology in China Iii: Biofuels and Bioenergy, vol. 128, 2012, pp. 1–24.

[8] E.T. Reese, Enzymatic hydrolysis of cellulose, Appl. Microbiol. 4 (1) (1956) 39–45.

[9] S.J. Horn, G. Vaaje-Kolstad, B. Westereng, V.G.H. Eijsink, Novel enzymes for the degradation of cellulose, Biotechnol. Biofuels 5 (2012).

[10] W.T. Beeson, V.V. Vu, E.A. Span, C.M. Phillips, M.A. Marletta, Cellulose degradation by polysaccharide monooxygenases, Annu. Rev. Biochem. 84 (84) (2015) 923–946.

[11] G. Vaaje-Kolstad, D.R. Houston, A.H.K. Riemen, V.G.H. Eijsink, D.M.F. van Aalten, Crystal structure and binding properties of the Serratia marcescens chitin-binding protein CBP21, J. Biol. Chem. 280 (12) (2005) 11313–11319.

[12] Z. Forsberg, G. Vaaje-Kolstad, B. Westereng, A.C. Bunaes, Y. Stenstrom, A. MacKenzie, M. Sorlie, S.J. Horn, V.G.H. Eijsink, Cleavage of cellulose by a CBM33 protein, Protein Sci. 20 (9) (2011) 1479–1483.

[13] R.J. Quinlan, M.D. Sweeney, L. Lo Leggio, H. Otten, J.C.N. Poulsen, K.S. Johansen, K.B.R.M. Krogh, C.I. Jorgensen, M. Tovborg, A. Anthonsen, T. Tryfona, C.P. Walter, P. Dupree, F. Xu, G.J. Davies, P.H. Walton, Insights into the oxidative degradation of cellulose by a copper metalloenzyme that exploits biomass components, Proc. Natl. Acad. Sci. U. S. A. 108 (37) (2011) 15079–15084.

[14] G. Vaaje-Kolstad, B. Westereng, S.J. Horn, Z.L. Liu, H. Zhai, M. Sorlie, V.G.H. Eijsink, An oxidative enzyme boosting the enzymatic conversion of recalcitrant polysaccharides, Science 330 (6001) (2010) 219–222.

[15] D. Cannella, C.W.C. Hsieh, C. Felby, H. Jorgensen, Production and effect of aldonic acids during enzymatic hydrolysis of lignocellulose at high dry matter content, Biotechnol. Biofuels 5 (2012).

[16] Novozymes, New Enzymes Turn Waste into Fuel, 2010.

[17] V. Lombard, H.G. Ramulu, E. Drula, P.M. Coutinho, B. Henrissat, The carbohydrate-active enzymes database (CAZy) in 2013, Nucleic Acids Res. 42 (D1) (2014) D490–D495.

[18] M. Couturier, S. Ladeveze, G. Sulzenbacher, L. Ciano, M. Fanuel, C. Moreau, A. Villares, B. Cathala, F. Chaspoul, K.E. Frandsen, A. Labourel, I. Herpoel-Gimbert, S. Grisel, M. Haon, N. Lenfant, H. Rogniaux, D. Ropartz, G.J. Davies, M.N. Rosso, P.H. Walton, B. Henrissat, J.G. Berrin, Lytic xylan oxidases from wood-decay fungi unlock biomass degradation, Nat. Chem. Biol. 14 (3) (2018) 306–310.

[19] F. Sabbadin, G.R. Hemsworth, L. Ciano, B. Henrissat, P. Dupree, T. Tryfona, R.D.S. Marques, S.T. Sweeney, K. Besser, L. Elias, G. Pesante, Y. Li, A.A. Dowle, R. Bates, L.D. Gomez, R. Simister, G.J. Davies, P.H. Walton, N.C. Bruce, S.J. McQueen-Mason, An ancient family of lytic polysaccharide monooxygenases with roles in arthropod development and biomass digestion, Nat. Commun. 9 (1) (2018) 756.

[20] K.E.H. Frandsen, L. Lo Leggio, Lytic polysaccharide monooxygenases: a crystallographer's view on a new class of biomass-degrading enzymes, Iucrj 3 (2016) 448–467.

[21] M. Gudmundsson, S. Kim, M. Wu, T. Ishida, M.H. Momeni, G. Vaaje-Kolstad, D. Lundberg, A. Royant, J. Stahlberg, V.G.H. Eijsink, G.T. Beckham, M. Sandgren, Structural and electronic snapshots during the transition from a Cu(II) to Cu(I) metal center of a lytic polysaccharide monooxygenase by X-ray photoreduction, J. Biol. Chem. 289 (27) (2014) 18782–18792.

[22] L. Schrödinger, The PyMOL Molecular Graphics System, Version 1.8, 2015.

[23] G. Courtade, R. Wimmer, A.K. Rohr, M. Preims, A.K.G. Felice, M. Dimarogona, G. Vaaje-Kolstad, M. Sorlie, M. Sandgren, R. Ludwig, V.G.H. Eijsink, F.L. Aachmann, Interactions of a fungal lytic polysaccharide monooxygenase with beta-glucan substrates and cellobiose dehydrogenase, Proc. Natl. Acad. Sci. U. S. A. 113 (21) (2016) 5922–5927.

[24] A.J. Book, R.M. Yennamalli, T.E. Takasuka, C.R. Currie, G.N. Phillips, B.G. Fox, Evolution of substrate specificity in bacterial AA10 lytic polysaccharide monooxygenases, Biotechnol. Biofuels 7 (2014).

[25] Z. Forsberg, A.K. Mackenzie, M. Sorlie, A.K. Rohr, R. Helland, A.S. Arvai, G. Vaaje-Kolstad, V.G.H. Eijsink, Structural and functional characterization of a conserved pair of bacterial cellulose-oxidizing lytic polysaccharide monooxygenases, Proc. Natl. Acad. Sci. U. S. A. 111 (23) (2014) 8446–8451.

[26] E.A. Span, M.A. Marietta, The framework of polysaccharide monooxygenase structure and chemistry, Curr. Opin. Struct. Biol. 35 (2015) 93–99.

[27] V.V. Vu, W.T. Beeson, C.M. Phillips, J.H.D. Cate, M.A. Marletta, Determinants of regioselective hydroxylation in the fungal polysaccharide monooxygenases, J. Am. Chem. Soc. 136 (2) (2014) 562–565.

[28] T. Isaksen, B. Westereng, F.L. Aachmann, J.W. Agger, D. Kracher, R. Kittl, R. Ludwig, D. Haltrich, V.G.H. Eijsink, S.J. Horn, A C4-oxidizing lytic polysaccharide monooxygenase cleaving both cellulose and cello-oligosaccharides, J. Biol. Chem. 289 (5) (2014) 2632–2642.

[29] A.R. Atilgan, S.R. Durell, R.L. Jernigan, M.C. Demirel, O. Keskin, I. Bahar, Anisotropy of fluctuation dynamics of proteins with an elastic network model, Biophys. J. 80 (1) (2001) 505–515.

[30] G. Li, A. Van Wynsberghe, O.N.A. Demerdash, Q. Cui, Normal mode analysis of macromolecules: from enzyme active sites to molecular machines, in: Q. Cui, I. Bahar (Eds.), Normal Mode Analysis:Theory and Applications to Biological and Chemical Systems, Chapman and Hall/CRC, New York, 2006, pp. 65–89.

[31] K. Hinsen, Analysis of domain motions by approximate normal mode calculations, Proteins Struct. Funct. Genet. 33 (3) (1998) 417–429.

[32] I. Bahar, A.R. Atilgan, B. Erman, Direct evaluation of thermal fluctuations in proteins using a single-parameter harmonic potential, Folding Des. 2 (3) (1997) 173–181.

[33] M.M. Tirion, Large amplitude elastic motions in proteins from a single-parameter, atomic analysis, Phys. Rev. Lett. 77 (9) (1996) 1905–1908.

[34] T. Haliloglu, I. Bahar, B. Erman, Gaussian dynamics of folded proteins, Phys. Rev. Lett. 79 (16) (1997) 3090–3093.

[35] S. Kundu, J.S. Melton, D.C. Sorensen, G.N. Phillips, Dynamics of proteins in crystals: comparison of experiment with simple models, Biophys. J. 83 (2) (2002) 723–732.

[36] H.M. Berman, J. Westbrook, Z. Feng, G. Gilliland, T.N. Bhat, H. Weissig, I.N. Shindyalov, P.E. Bourne, The protein Data Bank, Nucleic Acids Res. 28 (1) (2000) 235–242.

[37] K. Hinsen, Normal Mode Theory and Harmonic Potential Approximations, 2006, pp. 1–16.

[38] I. Bahar, A. Rader, J Coarse-grained normal mode analysis in structural biology, Curr. Opin. Struct. Biol. 15 (2005) 586–592.

[39] W. Humphrey, A. Dalke, K. Schulten, VMD: visual molecular dynamics, J. Mol. Graph. Model. 14 (1) (1996) 33–38.

[40] M. Wu, G.T. Beckham, A.M. Larsson, T. Ishida, S. Kim, C.M. Payne, M.E. Himmel, M.F. Crowley, S.J. Horn, B. Westereng, K. Igarashi, M. Samejima, J. Stahlberg, V.G.H. Eijsink, M. Sandgren, Crystal structure and computational characterization of the lytic polysaccharide monooxygenase GH61D from the basidiomycota fungus phanerochaete chrysosporium, J. Biol. Chem. 288 (18) (2013) 12828–12839.

[41] K.A. Borkovich, L.A. Alex, O. Yarden, M. Freitag, G.E. Turner, N.D. Read, S. Seiler, D. Bell-Pedersen, J. Paietta, N. Plesofsky, M. Plamann, M. Goodrich-Tanrikulu, U. Schulte, G. Mannhaupt, F.E. Nargang, A. Radford, C. Selitrennikoff, J.E. Galagan, J.C. Dunlap, J.J. Loros, D. Catcheside, H. Inoue, R. Aramayo, M. Polymenis, E.U. Selker, M.S. Sachs, G.A. Marzluf, I. Paulsen, R. Davis, D.J. Ebbole, A. Zelter, E.R. Kalkman, R. O'Rourke, F. Bowring, J. Yeadon, C. Ishii, K. Suzuki, W. Sakai, R. Pratt, Lessons from the genome sequence of Neurospora crassa: tracing the path from genomic blueprint to multicellular organism, Microbiol. Mol. Biol. Rev. 68 (1) (2004) 1–108.

[42] R.H. Davis, D.D. Perkins, Timeline: Neurospora: a model of model microbes, Nat. Rev. Genet. 3 (5) (2002) 397–403.

[43] J.C. Dunlap, K.A. Borkovich, M.R. Henn, G.E. Turner, M.S. Sachs, N.L. Glass, K. McCluskey, M. Plamann, J.E. Galagan, B.W. Birren, R.L. Weiss, J.P. Townsend, J.J. Loros, M.A. Nelson, R. Lambreghts, H.V. Colot, G. Park, P. Collopy, C. Ringelberg, C. Crew, L. Litvinkova, D. DeCaprio, H.M. Hood, S. Curilla, M. Shi, M. Crawford, M. Koerhsen, P. Montgomery, L. Larson, M. Pearson, T. Kasuga, C. Tian, M. Basturkmen, L. Altamirano, J. Xu, Enabling a community to dissect an organism: overview of the Neurospora functional genomics project, Adv. Genet. 57 (2007) 49–96.

[44] J.E. Galagan, S.E. Calvo, K.A. Borkovich, E.U. Selker, N.D. Read, D. Jaffe, W. FitzHugh, L.J. Ma, S. Smirnov, S. Purcell, B. Rehman, T. Elkins, R. Engels, S. Wang, C.B. Nielsen, J. Butler, M. Endrizzi, D. Qui, P. Ianakiev, D. Bell-Pedersen, M.A. Nelson, M. Werner-Washburne, C.P. Selitrennikoff, J.A. Kinsey, E.L. Braun, A. Zelter, U. Schulte, G.O. Kothe, G. Jedd, W. Mewes, C. Staben, E. Marcotte, D. Greenberg, A. Roy, K. Foley, J. Naylor, N. Stange-Thomann, R. Barrett, S. Gnerre, M. Kamal, M. Kamvysselis, E. Mauceli, C. Bielke, S. Rudd,

D. Frishman, S. Krystofova, C. Rasmussen, R.L. Metzenberg, D.D. Perkins, S. Kroken, C. Cogoni, G. Macino, D. Catcheside, W. Li, R.J. Pratt, S.A. Osmani, C.P. DeSouza, L. Glass, M.J. Orbach, J.A. Berglund, R. Voelker, O. Yarden, M. Plamann, S. Seiler, J. Dunlap, A. Radford, R. Aramayo, D.O. Natvig, L.A. Alex, G. Mannhaupt, D.J. Ebbole, M. Freitag, I. Paulsen, M.S. Sachs, E.S. Lander, C. Nusbaum, B. Birren, The genome sequence of the filamentous fungus Neurospora crassa, Nature 422 (6934) (2003) 859–868.

[45] K. Henzler-Wildman, D. Kern, Dynamic personalities of proteins, Nature 450 (7172) (2007) 964–972.

[46] A. Amadei, A.B.M. Linssen, H.J.C. Berendsen, Essential dynamics of proteins, Proteins Struct. Funct. Genet. 17 (4) (1993) 412–425.

[47] F.L. Aachmann, M. Sorlie, G. Skjak-Braek, V.G.H. Eijsink, G. Vaaje-Kolstad, NMR structure of a lytic polysaccharide monooxygenase provides insight into copper binding, protein dynamics, and substrate interactions, Proc. Natl. Acad. Sci. U. S. A. 109 (46) (2012) 18779–18784.

[48] O. Fisette, P. Lague, S. Gagne, S. Morin, Synergistic applications of MD and NMR for the study of biological systems, J. Biomed. Biotechnol. (2012), 254208. https://doi.org/10.1155/2012/254208.

[49] B. Liu, A.A. Kognole, M. Wu, B. Westereng, M.F. Crowley, S. Kim, M. Dimarogona, C.M. Payne, M. Sandgren, Structural and molecular dynamics studies of a C1-oxidizing lytic polysaccharide monooxygenase from Heterobasidion irregulare reveal amino acids important for substrate recognition, FEBS J. 285 (12) (2018) 2225–2242.

[50] A. Bakan, L.M. Meireles, I. Bahar, ProDy: protein dynamics inferred from theory and experiments, Bioinformatics 27 (11) (2011) 1575–1577.

[51] S.C. Xu, H.M. Han, W.W. Zhang, Q.Q. Zhang, R.Y. Long, H. Chen, Z.X. He, Analysis of regional contributions to the national carbon intensity in China in different Five Year Plan periods, J. Clean. Prod 145 (2017) 209–220.

Further reading

[52] J.P. Bacik, S. Mekasha, Z. Forsberg, A.Y. Kovalevsky, G. Vaaje-Kolstad, V.G.H. Eijsink, J.C. Nix, L. Coates, M.J. Cuneo, C.J. Unkefer, J.C.H. Chen, Neutron and atomic resolution X-ray structures of a lytic polysaccharide monooxygenase reveal copper-mediated dioxygen binding and evidence for N-terminal deprotonation, Biochemistry 56 (20) (2017) 2529–2532.

[53] A.S. Borisova, T. Isaksen, M. Dimarogona, A.A. Kognole, G. Mathiesen, A. Varnai, A.K. Rohr, C.M. Payne, M. Sorlie, M. Sandgren, V.G.H. Eijsink, Structural and functional characterization of a lytic polysaccharide monooxygenase with broad substrate specificity, J. Biol. Chem. 290 (38) (2015) 22955–22969.

[54] A.K. Chaplin, M.T. Wilson, M.A. Hough, D.A. Svistunenko, G.R. Hemsworth, P.H. Walton, E. Vijgenboom, J.A.R. Worrall, Heterogeneity in the histidine-brace copper coordination sphere in auxiliary activity family 10 (AA10) lytic polysaccharide monooxygenases, J. Biol. Chem. 291 (24) (2016) 12838–12850.

[55] E. Chiu, M. Hijnen, R.D. Bunker, M. Boudes, C. Rajendran, K. Aizel, V. Olieric, C. Schulze-Briese, W. Mitsuhashi, V. Young, V.K. Ward, M. Bergoin, P. Metcalf, F. Coulibaly, Structural basis for the enhancement of virulence by viral spindles and their in vivo crystallization, Proc. Natl. Acad. Sci. U. S. A. 112 (13) (2015) 3973–3978.

[56] Z. Forsberg, C.E. Nelson, B. Dalhus, S. Mekasha, J.S.M. Loose, L.I. Crouch, A.K. Rohr, J.G. Gardner, V.G.H. Eijsink, G. Vaaje-Kolstad, Structural and functional analysis of a lytic polysaccharide monooxygenase important for efficient utilization of chitin in cellvibrio japonicus, J. Biol. Chem. 291 (14) (2016) 7300–7312.

[57] K.E.H. Frandsen, J.C.N. Poulsen, T. Tandrup, L. Lo Leggio, Unliganded and substrate bound structures of the cellooligosaccharide active lytic polysaccharide monooxygenase LsAA9A at low pH, Carbohydr. Res. 448 (2017) 187–190.

[58] K.E.H. Frandsen, T.J. Simmons, P. Dupree, J.C.N. Poulsen, G.R. Hemsworth, L. Ciano, E.M. Johnston, M. Tovborg, K.S. Johansen, P. von Freiesleben, L. Marmuse, S. Fort, S. Cottaz, H. Driguez, B. Henrissat, N. Lenfant, F. Tuna, A. Baldansuren, G.J. Davies, L. Lo Leggio, P.H. Walton, The molecular basis of polysaccharide cleavage by lytic polysaccharide monooxygenases, Nat. Chem. Biol. 12 (4) (2016) 298–303.

[59] P.V. Harris, D. Welner, K.C. McFarland, E. Re, J.C.N. Poulsen, K. Brown, R. Salbo, H.S. Ding, E. Vlasenko, S. Merino, F. Xu, J. Cherry, S. Larsen, L. Lo Leggio, Stimulation of lignocellulosic biomass hydrolysis by proteins of glycoside hydrolase family 61: structure and function of a large, enigmatic family, Biochemistry 49 (15) (2010) 3305–3316.

[60] G.R. Hemsworth, B. Henrissat, G.J. Davies, P.H. Walton, Discovery and characterization of a new family of lytic polysaccharide monooxygenases, Nat. Chem. Biol. 10 (2) (2014) 122–126.

[61] G.R. Hemsworth, E.J. Taylor, R.Q. Kim, R.C. Gregory, S.J. Lewis, J.P. Turkenburg, A. Parkin, G.J. Davies, P.H. Walton, The copper active site of CBM33 polysaccharide oxygenases, J. Am. Chem. Soc. 135 (16) (2013) 6069–6077.

[62] S. Karkehabadi, H. Hansson, S. Kim, K. Piens, C. Mitchinson, M. Sandgren, The first structure of a glycoside hydrolase family 61 member, Cel61B from hypocrea jecorina, at 1.6 angstrom resolution, J. Mol. Biol. 383 (1) (2008) 144–154.

[63] X. Li, W.T. Beeson, C.M. Phillips, M.A. Marletta, J.H.D. Cate, Structural basis for substrate targeting and catalysis by fungal polysaccharide monooxygenases, Structure 20 (6) (2012) 1051–1061.

[64] L. Lo Leggio, T.J. Simmons, J.C.N. Poulsen, K.E.H. Frandsen, G.R. Hemsworth, M.A. Stringer, P. von Freiesleben, M. Tovborg, K.S. Johansen, L. De Maria, P.V. Harris, C.L. Soong, P. Dupree, T. Tryfona, N. Lenfant, B. Henrissat, G.J. Davies, P.H. Walton, Structure and boosting activity of a starch-degrading lytic polysaccharide monooxygenase, Nat. Commun. 6 (2015).

[65] S. Mekasha, Z. Forsberg, B. Dalhus, J.P. Bacik, S. Choudhary, C. Schmidt-Dannert, G. Vaaje-Kolstad, V.G.H. Eijsink, Structural and functional characterization of a small chitin-active lytic polysaccharide monooxygenase domain of a multi-modular chitinase from Jonesia denitrificans, FEBS Lett. 590 (1) (2016) 34–42.

[66] W.B. O'Dell, P.K. Agarwal, F. Meilleur, Oxygen activation at the active site of a fungal lytic polysaccharide monooxygenase, Angew. Chem. Int. Ed. 56 (3) (2017a) 767–770.

[67] W.B. O'Dell, P.D. Swartz, K.L. Weiss, F. Meilleur, Crystallization of a fungal lytic polysaccharide monooxygenase expressed from glycoengineered Pichia pastoris for X-ray and neutron diffraction, in: Acta Crystallographica Section F-Structural Biology Communications, vol. 73, 2017, pp. 70–78.

[68] E.A. Span, D.L.M. Suess, M.C. Deller, R.D. Britt, M.A. Marletta, The role of the secondary coordination sphere in a fungal polysaccharide monooxygenase, ACS Chem. Biol. 12 (4) (2017) 1095–1103.

[69] G. Vaaje-Kolstad, L.A. Bohle, S. Gaseidnes, B. Dalhus, M. Bjoras, G. Mathiesen, V.G.H. Eijsink, Characterization of the chitinolytic machinery of Enterococcus faecalis V583 and high-resolution structure of its oxidative CBM33 enzyme, J. Mol. Biol. 416 (2) (2012) 239–254.

[70] E. Wong, G. Vaaje-Kolstad, A. Ghosh, R. Hurtado-Guerrero, P.V. Konarev, A.F.M. Ibrahim, D.I. Svergun, V.G.H. Eijsink, N.S. Chatterjee, D.M.F. van Aalten, The Vibrio cholerae colonization factor GbpA possesses a modular structure that governs binding to different host surfaces, PLoS Pathog. 8 (1) (2012).